DOI:10.1002/ejic.201300359

Linear Metallopolymers from Ruthenium(II)-2,6-di(quinolin-8-yl)pyridine Complexes by Electropolymerization – Formation of Redox-Stable and Emissive Films

Christian Friebe,[a,b] Helmar Görls,[c] Michael Jäger,*[a,b] and Ulrich S. Schubert*[a,b]

Keywords: Electropolymerization / Ruthenium / N ligands / Thin films / Density functional calculations

Two rodlike ruthenium(II) complexes of 2,6-di(quinolin-8-yl)-pyridines (dqp) were synthesized and possess a pair of 2-thienyl moieties attached to the 4-positions of the quinoline units of one ligand or at the 4-positions of the pyridine rings of both ligands. The heteroleptic and homoleptic complexes were characterized by UV/Vis absorption and emission spectroscopy as well as electrochemical and X-ray crystallographic means. The subsequent electropolymerization of the thiophene units led to the controlled formation of thin solid films onto electrode surfaces as proven by X-ray photoelectron spectroscopy (XPS). The electrochemical analysis of the films was complemented by UV/Vis spectroscopy and UV/Vis/NIR spectroelectrochemistry, which revealed their stability towards oxidation, red emission, and reversible redox switching of their optical properties. Density functional theory (DFT) calculations were executed on the monomer complexes and respective dimeric systems to gain insight into their spectroscopic and electrochemical properties.

Introduction

Ruthenium(II) polypyridyl complexes are favorable building units for photophysical applications, in particular as sensitizers within light-harvesting devices, because of their ability to undergo efficient and long-lived light-induced charge separation.[1] The prototypical $Ru(bpy)_3^{2+}$ (bpy = 2,2′-bipyridine) shows a long excited-state lifetime of 860 ns, which allows subsequent redox reactions to occur.[2] However, the tris(bidentate) ligand assembly can lead to the formation of enantiomeric and diastereomeric mixtures and impedes the ideal *trans* arrangement of donor and acceptor moieties with maximal separation to prevent back-reactions.[3] On the other hand, the bis(tridentate) congener $Ru(tpy)_2^{2+}$ (tpy = 2,2′:6′,2′′-terpyridine) allows for the stringent *trans* alignment of the substituents,[4] but possesses a very short excited-state lifetime of 0.25 ns, which precludes efficient utilization of the excited states.[5] The observed short lifetimes are caused by the efficient interaction of the triplet metal-to-ligand charge-transfer (^{3}MLCT) excited state with the triplet metal-centered (^{3}MC) states and their fast and radiationless deactivation towards the singlet ground state within $Ru(tpy)_2^{2+}$ and analogous systems.[6]

The different strategies to overcome this limitation mainly focus on the enlargement of the ^{3}MLCT–^{3}MC energy gap by stabilization of the ^{3}MLCT state, destabilization of the ^{3}MC state, or both. The most promising approaches are based on the incorporation of strong electron donors by cyclometalation[6a,7] or N-heterocyclic carbenes[8] and structural modifications,[9] whereas the attachment of additional energy-storing chromophores only enhances the apparent lifetime.[10] Hammerström et al. demonstrated that the utilization of tridentate ligands with a bite angle of 180° leads to a less distorted octahedral complex geometry, which causes a decreased admixing of metal d orbitals into the lowest unoccupied molecular orbital (LUMO). Thus, the orbital overlap between the ligand-centered LUMOs and the e_g orbitals is diminished and a deactivation via the ^{3}MC state becomes less probable.[6b] Applying this concept, the family of substituted $Ru(dqp)_2^{2+}$-based complexes [dqp = 2,6-di(quinolin-8-yl)pyridine] combines excellent properties for light-harvesting applications with an excited-state lifetime in the µs time scale.[11]

The subsequent incorporation into photovoltaic devices requires thin-film processing of the respective sensitizers, that is, the deposition of a layer that is thin and homogen-

---

[a] Laboratory of Organic and Macromolecular Chemistry (IOMC), Friedrich Schiller University Jena,
Humboldtstr. 10, 07743 Jena, Germany
E-mail: michael.jager.iomc@uni-jena.de
ulrich.schubert@uni-jena.de
Homepage: http://www.schubert-group.com/
[b] Jena Center for Soft Matter (JCSM), Friedrich Schiller University Jena,
Philosophenweg 7, 07743 Jena, Germany
[c] Laboratory of Inorganic and Analytic Chemistry (IAAC), Friedrich Schiller University Jena,
Lessingstr. 8, 07743 Jena, Germany

Supporting information for this article is available on the WWW under http://dx.doi.org/10.1002/ejic.201300359.

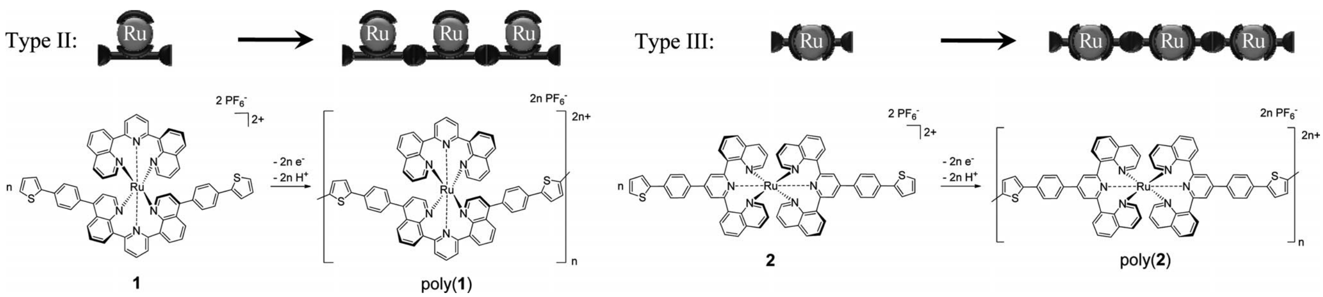

Scheme 1. Type II and type III arrangement of metal-containing polymers as applied for Ru(dqp)$_2^{2+}$ complexes in this contribution.

eous enough to allow efficient charge transport onto an electrode surface. For this purpose, a convenient and widespread technique is the electrochemical polymerization of a metal-containing monomer solution to enable the direct preparation of an insoluble polymeric coating on the surface[12] and, thus, numerous ruthenium(II) polypyridyl-type complexes have been processed by electropolymerization.[13] In this contribution, we present two Ru(dqp)$_2^{2+}$ complexes featuring 2-thienyl units linked either to the quinoline (**1**) or the pyridine moieties (**2**) and their subsequent incorporation into a photoactive film by electropolymerization (Scheme 1). The two investigated substitution patterns enable a lateral attachment to the polymer main chain or a direct incorporation into the backbone (metal-containing polymers of type II and III, respectively, Scheme 1)[14] with equal spatial separation of the ruthenium(II) centers. First density functional theory (DFT) and time-dependent DFT (TD-DFT) calculations were performed to explore the structural, spectroscopic, and electrochemical properties of the designed systems. The second part describes the synthesis and characterization of the monomer complexes as well as the resulting polymer films by UV/Vis spectroscopy and cyclic voltammetry. Additionally, X-ray crystallographic analysis for the monomers and UV/Vis/NIR spectroelectrochemical experiments and X-ray photoelectron spectroscopy (XPS) studies of the obtained polymer films were executed.

Results and Discussion

DFT Calculations

DFT and TD-DFT calculations were performed to investigate the electronic structures and transitions of the two different conjugation paths. Firstly, the geometries of the complexes were optimized with the given charge and multiplicity and subsequently confirmed by vibrational analysis. The optical properties were further investigated by TD-DFT to obtain absorption spectra. In addition to the monomers, the respective dimetallic complexes were investigated to explore the effect of dimerization on the electronic structure (for optimized geometries, see Supporting Information).

The structural features of the complexes closely resemble those previously obtained for the parent Ru(dqp)$_2^{2+}$ with a different basis set (see Supporting Information).[11b] Notably, both substitution patterns differ in the degree of coplanarity (dihedral angle) between the dqp and the outer phenyl ring, which suggests an increased interaction with the dqp-based molecular orbitals (MOs) from **1** (49°) to **2** (30°). However, no significant differences between the phenyl and thiophene twists were observed (a comparison to the experimental data is provided below). The related dimeric complexes display very similar structural parameters and have identical Ru–N bond lengths and torsional angles. The twist between the phenyl and thiophene unit is slightly smaller, whereas the torsion angle between the bridging thiophene units is 10°. On the basis of the dihedral angles, phenyl–bithiophene–phenyl conjugation within the bridge is reasonable ($<22°$) and also allows coupling to the Ru(dqp)$_2^{2+}$ fragments ($<49°$).

The frontier MO energies and respective contributions of the involved fragments of the complexes in the ground state are depicted in the Supporting Information. Importantly, the highest occupied molecular orbitals (HOMO and HOMO–1) are mainly metal-based, whereas the nearby orbitals (HOMO–2 and HOMO–3) show significant admixing of the thiophene units. The lowest unoccupied molecular orbitals (LUMO to LUMO+5) are primarily localized on the dqp ligands. For the asymmetric complex **1**, the contribution of the thiophene-substituted dqp fragment to the LUMO and LUMO+1 is larger than that of nonfunctionalized dqp, whereas the opposite holds for the LUMO+2 and LUMO+3. For the symmetric complex **2**, the contribution of each dqp ligand to the LUMOs is equal because of the symmetry of the molecule. Upon dimerization, the orbital energy of the bithiophene fragments is significantly lowered and constitutes the new HOMO with only minor admixing of d orbitals from both ruthenium centers. However, the lower occupied orbitals remain metal-based. The LUMOs of the dimers are ligand-based and display a higher contribution of the dqp fragment connected to the bridge. The electronic structure of the complexes can be qualitatively summarized as follows: (1) The HOMO manifold is essentially ruthenium-based, (2) the dimers show a delocalized HOMO on the bridge with minor contributions of both metal centers, (3) the LUMO manifold is ligand-

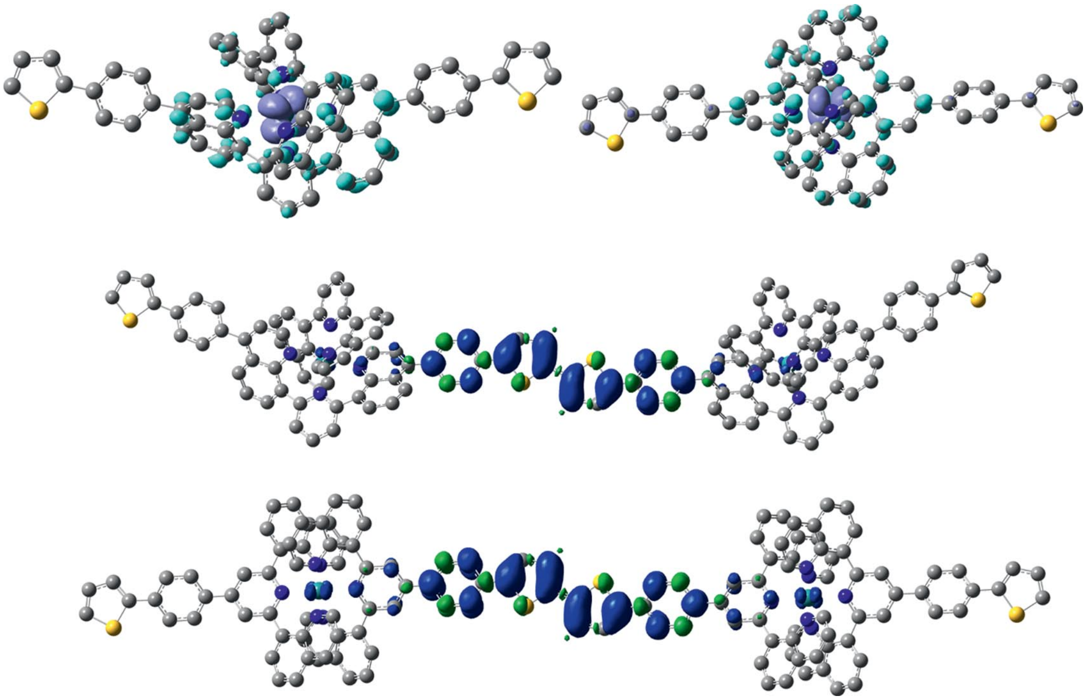

Figure 1. EDDM plots of the lowest-energy ground state absorptions (isovalue = 0.0016, decrease in blue, increase in cyan) of **1** (top left) and **2** (top right). Electron density from spin-density difference calculations of dimer(**1**) (middle) and dimer(**2**) (bottom, isovalue = 0.001) in the singly oxidized state.

based throughout the series and shows a larger contribution from the substituted dqp ligand. However, the computational results of the HOMOs of the dimers should be interpreted with care owing to the well-known artificial stabilization of delocalized states.[15]

The vertical excitations were investigated by TD-DFT calculations (see Supporting Information). Electron-density difference maps (EDDM) are often used to visualize electronic redistribution,[16] in particular if the discussion is complicated by many contributing MOs. The monomers **1** and **2** display low-energy transitions with MLCT character (Figure 1), whereas the higher-energy transitions revealed an extended delocalization across the aromatic units and an increased admixing of thiophene-based orbitals. Furthermore, the EDDM analysis shows the principle effect of the substitution pattern. The alignment of the thiophene- and metal-based d orbitals leads to higher oscillator strengths of the respective transitions. For complex **1**, this combination is less favorable and the strong MLCT transition is found at 505 nm, whereas this transition in complex **2** shows a pronounced redshift to 536 nm, in line with the lower dihedral angle between the dqp fragment and the phenyl ring (see above).

The dimers display a similar behavior, except for an additional very intense intraligand charge-transfer (ILCT) transition of the bis(thiophene). For dimer(**1**), the asymmetric substitution pattern induces a localization on the quinoline unit connected to the bridge, whereas the accepting LUMO of dimer(**2**) is almost evenly distributed over both dqp ligands. This behavior is consistent with the more efficient conjugation through the metal-based d orbitals in dimer(**2**), as described above.

The changes in the electronic structures of the complexes upon oxidation were examined by spin-density difference plots (see Supporting Information). Upon oxidation of the monomeric complexes, the first electron is removed from a metal-centered orbital, whereas the second one originates from one 4-(2-thienyl)phenyl unit. Hence, the intended redox-mediated coupling becomes reasonable upon a second oxidation, according to the accepted mechanism involving an oxidized thiophene radical.[17] In contrast, both dimers show first oxidations that reside primarily on the bridge with minor contributions from both ruthenium centers. The second and third oxidation processes are localized on the individual ruthenium centers (see Supporting Information).

Notably, the order of the successive oxidation steps may be reversed, owing to the discussed artificial stabilization of delocalized states.[15] However, the observed low energetic differences between the metal- and bridge-based orbitals as well as their spatial overlap suggest significant interactions between them.

The combined computational results of the monomeric and dimeric structures show their promising potential in electropolymerized films. As the polymerization process is expected to start upon the oxidation of the thiophene unit, the (easier) ruthenium-centered oxidation may serve as a valuable tool to monitor the course of the electropolymerization. The MO analysis of the dimeric structures reveals an extended delocalization across the bridge, that is, a weak communication between the two metal centers in the oxidized state, which is beneficial for efficient charge migration within the films. However, a more detailed analysis, for example, modeling of polymeric structures, is beyond the scope of this study.

Syntheses of Monomers

The synthetic strategy towards the electropolymerizable thiophene-equipped complexes is shown in Scheme 2 and is based on the synthesis of the bromo-functionalized ligands, followed by the stepwise coordination to ruthenium, and the introduction of the thiophene moieties in the final step. This sequence was chosen to prevent any side reactions of the thiophene units owing to the harsh conditions during the coordination steps and to enable easy removal of the small amounts of the inevitably formed facial isomers by crystallization. In addition, this route also explores the versatility of the intermediate bromo complex, for example, for subsequent cross-coupling reactions. To construct the framework of the quinoline-functionalized ligand, the original route by C–C coupling was adjusted to tolerate the reactive peripheral bromo substituents. In this regard, 2-nitrobenzoic acid represents a valuable quinoline precursor, as shown by the efficient decarboxylative cross coupling with a variety of aryl halides.[18] To suppress the protonation of the formal C nucleophile after decarboxylation, the potassium salt was used instead.[19] The twofold coupling with 2,6-dibromopyridine gave **3** (48% yield), which was subsequently reduced to the corresponding bis(aniline) **4** by using hydrazine hydrate and palladium on charcoal. Finally, the quinoline ring formation was achieved by a twofold Skraup reaction with a commercial bromophenyl-substituted C_3 synthon.[20] Although this route gave only a low yield (15%) of bis(bromophenyl)-substituted dqp (**5**), it is comparable with related single Skraup reactions and benefits from the direct access to the bis-functionalized ligand. The related pyridine-substituted ligand 8,8′-[4-(4-bromophenyl)pyridine-2,6-diyl]diquinoline was synthesized by a Kröhnke reaction of acetylquinoline and *p*-bromobenzaldehyde as described in the literature.[21] The next step involved the coordination to a suitable ruthenium precursor and separation from facial isomers[11a] by fractionalized crystallization. Heating ligand **5** with $[Ru(dqp)(CH_3CN)_3](PF_6)_2$ afforded complex **6** in excellent yield (95%). The subsequent conversion to the thiophene-functionalized complex (**1**) was quantitative without any detectable debromination according to the ^1H NMR signal intensity ratios of the thiophene- and the quinoline-related protons. The related homoleptic complex **2** was synthesized in a similar stepwise fashion; the initial reaction of $RuCl_3$ with 8,8′-[4-(4-bromophenyl)pyridine-2,6-diyl]diquinoline was followed by a reduction and halide abstraction with Ag^I to yield the intermediate complex **7**. The next step is the coordination of a second equivalent of 8,8′-[4-(4-bromophenyl)pyridine-2,6-diyl]diquinoline; however, some debromination occurred and isolation of the bis(bromo) complex by chromatography and crystallization failed. We tentatively assign this failure to the small structural difference between the H and Br substituents among the complexes. Hence, the crude material was converted into the thiophene-equipped complexes, which were successfully separated by crystallization. The origin of the unexpected debromination is unknown and the isolated yields of **2** are lower (38% over both steps).

The ^1H NMR spectra of **1** and **2** show the characteristic pattern of the coordinated ligands in the aromatic region (Figure 2) and are supported by 2D NMR spectroscopic data (see Supporting Information). The spectrum of the asymmetric complex **1** has two overlapping sets of signals for each ligand. However, the subunits can be identified according to their characteristic chemical shifts and coupling

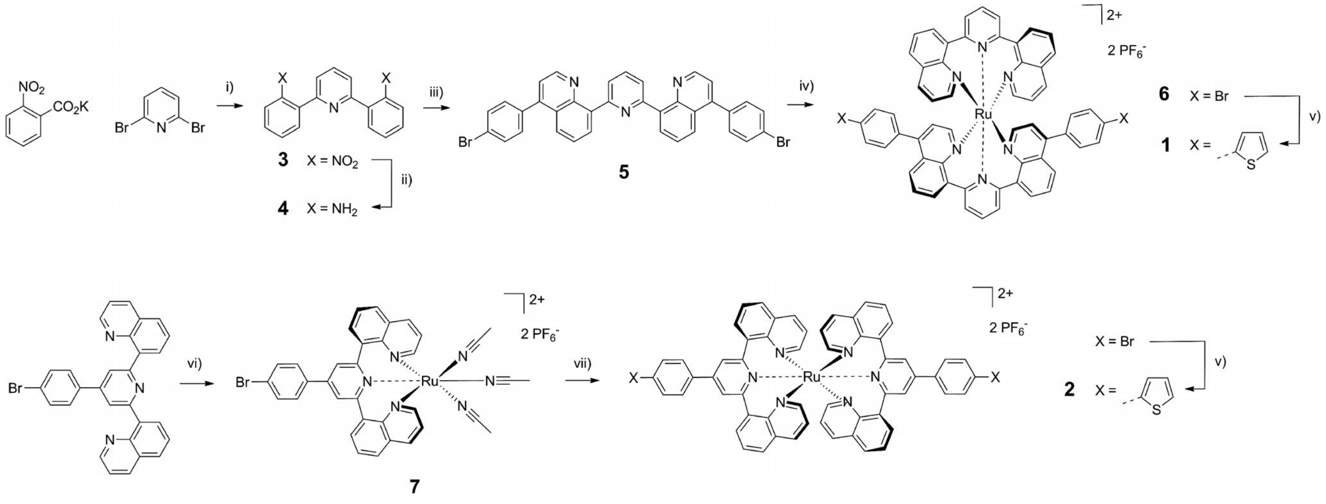

Scheme 2. Schematic representation of the synthetic route towards the heteroleptic complex **1** (top) and the homoleptic complex **2** (bottom): (i) CuI, Pd/C, 1,10-phenanthroline, *N*-methyl-2-pyrrolidinone (NMP), 180 °C, 15 h, 48%; (ii) Pd/C, hydrazine hydrate, EtOH, 80 °C, 1 h, 86%; (iii) 1-(4-bromophenyl)-3-chloropropan-1-one, arsenic pentoxide, phosphoric acid, 140 °C, 2 h, 15%; (iv) $[Ru(dqp)(CH_3CN)_3](PF_6)_2$, ethylene glycol, 140 °C, 14 h, 95%; (v) thiophen-2-ylboronic acid, $Pd(dba)_2$, S-PHOS, CH_3CN/H_2O, potassium carbonate, 100 °C, 16 h, 92 (**1**) and 55% (**2**); (vi) 1. $RuCl_3 \cdot 3H_2O$, EtOH, 115 °C, 13 h; 2. $AgNO_3$, $CH_3CN/EtOH/H_2O$, 90 °C, 17 h, then NH_4PF_6, 60%; (vii) 8,8′-[4-(4-bromophenyl)pyridine-2,6-diyl]diquinoline, ethylene glycol, 140 °C, 14 h, 68%.

patterns, in agreement with the literature.[11a,21] The proton in the 3-position of the quinoline unit is noticeable as a doublet in ligand **5** or as a double doublet in unsubstituted dqp. The protons in the 4-position of the pyridine rings appear as overlapping triplets owing to a small chemical shift difference. Two of the thiophene protons are well resolved and can be used to validate the thiophene content. A direct comparison by means of the adjacent phenyl ring is complicated owing to superposition with the remaining signals. Complex **2** shows a less complicated spectrum owing to the axial symmetry of the molecule. Similar features of the quinoline and thiophene units are present, whereas the 3- and 5-protons of the pyridine rings appear as singlets in the spectrum.

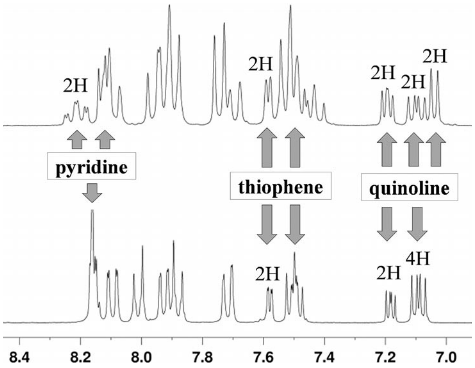

Figure 2. ^{1}H NMR spectra (CD_3CN, 300 MHz, expanded region) of **1** (top) and **2** (bottom) with assignment of the characteristic protons.

X-ray Crystallography

The structures of the complexes with both substitution patterns were also investigated by X-ray crystal analysis (Figure 3 and Table 1). All attempts to crystallize complex **1** gave only plates, and the quality of the collected X-ray data was not sufficient to allow discussion of the structure beyond the configuration and conformation (see Supporting Information). Hence, the related bromo precursor **6** was also investigated to supplement the structural discussion with respect to **2**. The geometrical features of the coordination site, that is, the mutual arrangement of the N and Ru atoms, are preserved in comparison to the parent Ru(dqp)$_2^{2+}$. Reinvestigation of the available X-ray data of Ru(dqp)$_2^{2+}$ showed a large deviation between the two complexes within the unit cell,[11b] which is seen in the large absolute difference of the respective bond lengths. However, the average value agrees well with the numbers derived from complexes **6** and **2**. In general, the Ru–N bond length of the central pyridine ring is shortened by 0.026 Å compared with that of the outer quinoline unit. A similar behavior was found for the calculated structures, despite the known typical overestimation of the calculated bond lengths (+0.04 Å). The internal N–Ru–N angles are all close to the ideal octahedral coordination, as are the dihedral angles between the quinoline and pyridine unit as calculated from their respective mean planes.

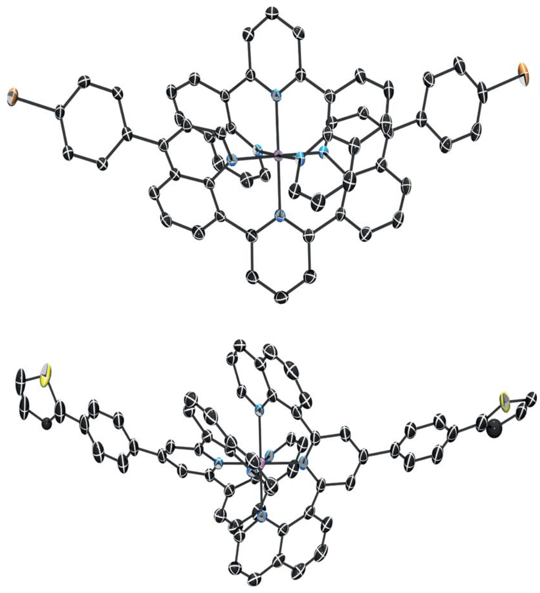

Figure 3. Top: Solid-state structure of **6** (ellipsoids drawn at 50% probability, hydrogen atoms are omitted for clarity). Bottom: Solid-state structure of **2** (ellipsoids drawn at 50% probability, hydrogen atoms are omitted and only one conformation of the thiophene units is displayed for clarity, spherical carbon atoms are isotropic).

The numbers agree well with those of the computed structures (37°); somewhat larger variations were found for **2**. This observation is tentatively attributed to crystal packing effects and indicates a certain flexibility of the coordinated ligand. This distortion is also visible from the "bending" away from the C_2 axis of the molecule in **2** (Figure 3). In addition, two conformations of the thiophene unit with respect to the neighboring phenyl group were found in the solid state and arise from the very similar steric demand

Table 1. Solid-state structural data for Ru(dqp)$_2^{2+}$, **6**, and **2**.

Compound	Ru–N[a] [Å] dqp–thiophene[b] N^{py}	 N^{quin}	 dqp N^{py}	 N^{quin}	N–Ru–N [°] Adjacent	 Axial	Torsion angle[c] [°] py–quin	 py–ph	 ph–tph
Ru(dqp)$_2^{2+}$[d]	–	–	2.034 (0.030)	2.063 (0.050)	88–92	176–180	35–40	–	–
6	2.036 (–)	2.073 (0.002)	2.039 (–)	2.070 (0.005)	89–90	179–180	37–41	46–47	4–33[e]
2	2.028 (–)	2.064 (0.007)	–	–	89–91	179–180	29–44	26	13

[a] Numbers in parentheses are the absolute differences between the experimental minimum and maximum values. [b] Thiophene-containing ligand {i.e., **3** or 8,8′-[4-(4-bromophenyl)pyridine-2,6-diyl]diquinoline}. [c] Calculated angles spanned by the mean planes defined by all heteroatoms of the aromatic unit (py = pyridine, quin = quinoline, ph = phenyl, tph = thiophene). [d] Calculated from the crystallographic data (average of both complexes of the unit cell) from ref.[11b] [e] Data taken from the structural motif of **1**.

after a 180° rotation along the connecting C–C bond. The structural motif of **1** displays a similar torsion angle between the pyridine and phenyl rings (45°) as that in **6**, but a large variation for the phenyl and thiophene unit (4 and 33°). The average experimental values agree very well with the DFT calculations; however, the larger numerical variations, for example, between the pyridine and quinoline units and the peripheral aromatic units, may be induced by the crystal packing (see Supporting Information).

Photophysical and Electrochemical Characterization of Monomers

The monomeric complexes were further characterized by UV/Vis spectroscopy (Figure 4 and Table 2). The absorption spectrum of the heteroleptic complex **1** shows characteristic bands between 400 and 600 nm, which are assigned to MLCT transitions. Complex **2** exhibits similar absorption bands, but displays a pronounced shoulder at longer wavelength and an additional peak at 425 nm. The experimental absorption data are in very good agreement with the DFT results (see also the electronic transitions in the DFT Calculations section). The UV/Vis emission measurements revealed structureless room-temperature emission bands at 698 (**1**) and 678 nm (**2**) with Stokes shifts of 4900 and 3300 cm^{-1}, respectively, which indicate significant differences between the two conjugation pathways in the emissive excited states. Furthermore, photoluminescence quantum yields (Φ_{PL}) of 0.8 and 3.1% for **1** and **2**, respectively, could be determined in deaerated solutions at room temperature. The excitation spectra support the assignments and agree with the reported data of the parent Ru(dqp)$_2^{2+}$ complex.[11b]

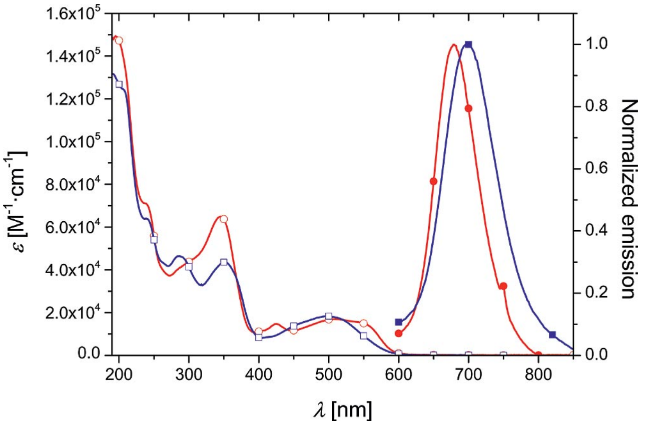

Figure 4. UV/Vis absorption (hollow symbols) and emission (filled symbols) spectra of the monomeric complexes **1** (blue) and **2** (red) (10^{-6} M in CH_3CN).

Cyclic voltammetric (CV) measurements (Table 2 and Supporting Information) showed reversible first oxidations at 0.70 V vs. Fc$^+$/Fc for **1** and 0.67 V for **2**, which are attributed to single-electron Ru^{III}/Ru^{II} redox processes. A second, irreversible oxidation wave was observed at ca. 1.3 V for both complexes and is assigned to the formation of thiophene radical moieties. Furthermore, the first reduction signals at ca. –1.70 V featured reversible behavior for both complexes.

The optical changes of **1** and **2** upon oxidation were investigated by UV/Vis/NIR spectroelectrochemistry. Firstly, a decrease of the MLCT absorption band at 500 nm was observed as well as the formation of a broad absorption band between 600 and 1100 nm featuring several unassigned low-energy transitions from lower-lying occupied orbitals to the metal-based singly occupied molecular orbital (SOMO, see the Supporting Information). These results are in line with those for the parent Ru(dqp)$_2^{2+}$ and are further discussed with regard to the electropolymerized films (see below).

Electropolymerization

Complex **1** was electropolymerized in acetonitrile containing 5 vol.-% $BF_3{\cdot}OEt_2$ and 0.1 M Bu_4NPF_6 as conductive electrolyte, according to the proposed reaction in Scheme 1. The electropolymerization was not possible in pure acetonitrile/Bu_4NPF_6. Hence, the Lewis acid boron trifluoride diethyl etherate was used as it interacts with the aromatic system of the thiophene and reduces its aromaticity and, thus, leads to a lowered oxidation potential for the thiophene moieties and enables electropolymerization.[22] The polymerization was conducted potentiodynamically by cycling between –0.5 and 1.7 V vs. Fc$^+$/Fc; the thiophene moieties are oxidized at ca. 1.2 V to form reactive thienyl cation radicals.[17] Figure 5 shows the development of the cyclic voltammogram over the first 50 cycles: It exhibits a well-defined growth of the characteristic electrochemical response at 0.7 V, and the signal corresponding to oxidation of the mono-thiophene decreases over the first cycles owing to the consumption of monomeric complexes near the electrode surface. Notably, a small cathodic peak at ca. 0.9 V occurs after two cycles and is tentatively assigned to the re-reduction of oxidized thiophene moieties, which may originate from trapped units within the (formed) film or from

Table 2. UV/Vis spectroscopic properties and electrochemical data of the monomer complexes (in CH_3CN, 10^{-6} M for UV/Vis spectroscopy, 10^{-4} M with 0.1 M Bu_4NPF_6 for electrochemistry).

	λ_{Abs} [nm] (ε [10^3 M^{-1} cm^{-1}])[a]	λ_{Em} [nm]	Φ_{PL}[b] [%]	$E_{1/2}$[c] [V] (i_{pa}/i_{pc}, ΔE_p [mV]) $2^+ \rightarrow 3^+$	$2^+ \rightarrow 1^+$
1	521s (16.6), 500 (18.5), 350 (43.9), 285 (46.4)	698	0.8	0.70 (1.05, 70)	–1.68 (0.94, 79)
2	553s (15.0), 507 (17.1), 425 (14.7), 345 (64.7), 290 (41.7)	678	3.1	0.67 (1.06, 68)	–1.70 (0.90, 73)

[a] s = shoulder. [b] Measured by using $[Ru(dqp)_2](PF_6)_2$ (Φ_{PL} = 2% in MeOH/EtOH, 1:4) as reference.[11b] [c] Measured vs. Fc$^+$/Fc.

unreacted units owing to a decrease in the rate of oxidative dimerization as the monomer is depleted. The increase of the peak current corresponding to the ruthenium(II)- and/or bis(thiophene) oxidation shows a slope change around the fifteenth cycle, most likely because of the complete coverage of the electrode surface with polymer, and, thus, a decreased charge transport, which causes a diminished polymerization rate.[23]

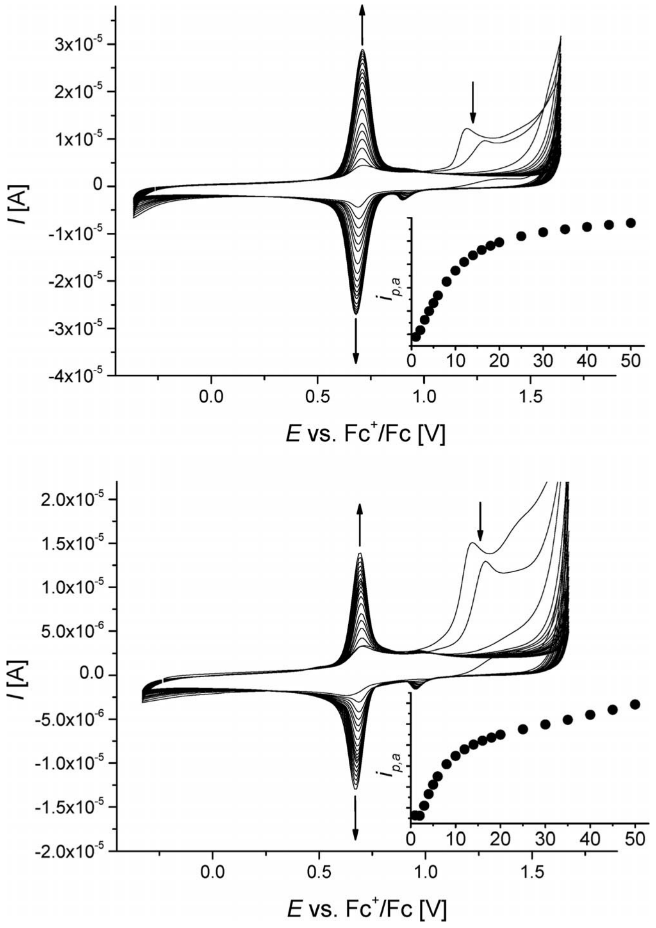

Figure 5. First 50 CV cycles of the electropolymerization of **1** (top) and **2** (bottom) on a glassy carbon disk electrode. Insets: Peak current increase at 0.70 V with cycle number (10^{-4} M in CH_3CN with 5 vol.-% $BF_3{\cdot}OEt_2$ and 0.1 M Bu_4NPF_6).

Likewise, electropolymerization of homoleptic **2** was performed and monitored by recording the respective cyclic voltammograms (Figure 5). As for the heteroleptic counterpart, a decrease of the current slope is observable at around the fifteenth cycle, but is less pronounced than for **1**. However, further studies are required to reveal the effect of other factors, such as counterion diffusion and charge mobility, on the film growth.

The elemental composition of the deposited films on indium tin oxide (ITO) coated glass substrates was investigated by X-ray photoelectron spectroscopy (XPS, see Supporting Information). Analysis of the spectra revealed the signals for the expected characteristic elements (namely, ruthenium, carbon, nitrogen, and sulfur) as well as Ru/S ratios of 1:2.1 and 1:1.9 for poly(**1**) and poly(**2**), respectively, consistent with the theoretical value.

The obtained CV data prove a successful electrochemical polymerization process and show a continuous growth of the peak current of the redox wave of the ruthenium(II) complex. This is attributed to deposition of the complex moieties and is accompanied by the disappearance of the thienyl-related signal, which is assigned to irreversible consecutive reactions of the formed thienyl radical cations, namely coupling reactions to generate oligomeric and polymeric chains. The utilization of boron trifluoride diethyl etherate, which is known to enhance the oxidative electropolymerization ability of aromatics by lowering of the redox potential, was necessary to enable the polymerization process.

Electrochemical and Photophysical Characterization of the Polymers

The films were rinsed with pure solvent to remove soluble monomer species after electropolymerization, and the coated working electrodes were immersed in fresh solvent with 0.1 M Bu_4NPF_6 and showed no dissolution at all. The electrochemical and photophysical data are summarized in Table 3. Figure 6 shows cyclic voltammograms of the oxidation of the polymers at different scan rates. The half-wave potential of poly(**1**) is only marginally shifted (towards 0.76 V vs. Fc^+/Fc) compared to that of the dissolved monomer complex. However, the involvement of the bis(thiophene) unit in the oxidation process cannot be excluded as the respective potential of the bis(phenylthienyl) (1.14 V vs. SCE, ca. 0.73 V vs. Fc^+/Fc)[24] is close to the observed redox potential. Furthermore, the redox process is reversible: The charge density is the same for oxidation and reduction (ca. $5 \times 10^{-4}\,C\,cm^{-2}$). The linear relationship between peak current and applied scan rate up to $500\,mV\,s^{-1}$ indicates the formation of a conductive film with redox processes that are only weakly limited by charge diffusion.[17,25] For poly(**2**), the oxidation signal appears well-defined and reversible (charge transfer of around $3 \times 10^{-4}\,C\,cm^{-2}$ for both oxidation and subsequent reduction) at a potential of 0.72 V vs. Fc^+/Fc. In contrast to poly(**1**), the linearity of the peak-current–scan-rate function is retained up to the maximum applied scan rate of $2000\,mV\,s^{-1}$ (Figure 6). This behavior can be explained by a higher charge mobility than in poly(**1**), which is further supported by the smaller E_{pa}–E_{pc} separation as well as the already mentioned smaller de-

Table 3. UV/Vis spectroscopic and electrochemical data of electropolymerized films.

	$\lambda_{Abs,\ poly}$ [nm]	$\lambda_{Abs,\ mono}$[a] [nm]	$\lambda_{Em,\ poly}$ [nm]	$\lambda_{Em,\ mono}$[a] [nm]	$E_{1/2,ox}$[b] [V]
Poly(**1**)	537	527	767	746	0.76
Poly(**2**)	567	551	745	717	0.72

[a] UV/Vis properties of spin-coated films of the monomer complexes. [b] Measured vs. Fc^+/Fc.

crease of the current slope during electropolymerization for poly(**2**).

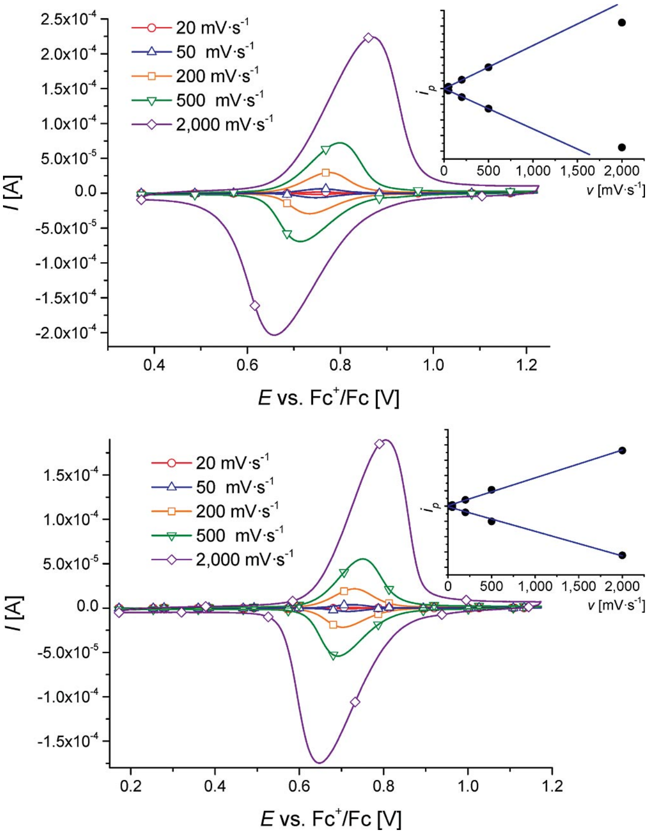

Figure 6. Cyclic voltammograms of the electropolymerized film of poly(**1**) (top) and poly(**2**) (bottom) at different scan rates. Insets: Peak-current dependence on scan rate [coated glassy carbon electrode in CH_3CN with 0.1 м Bu_4NPF_6; linear fit for poly(**1**) is valid up to 500 mV s^{-1}].

The UV/Vis absorption and emission characteristics of films of poly(**1**) and poly(**2**) on ITO-coated glass substrates were determined. The films of poly(**1**) and its respective monomer **1** (Figure 7) show a significant redshift of absorption of about 1400 and 1000 cm^{-1}, respectively, in comparison to that of the monomer dissolved in acetonitrile, but there are only marginal differences between the monomer and the polymer in the solid state. Similarly, the thin-film absorption of poly(**2**) exhibits a large redshift between the dissolved monomer complex **2** and the spin-coated film thereof, and only a small shift of 500 cm^{-1} occurs for the polymer relative to the monomer film (Figure 7). Furthermore, the additional peak at 425 nm, which was observed for **2** in solution, is also present for the films as an absorption shoulder at ca. 430 nm. Notably, the absorbance of the formed bis(phenylthienyl) moieties is expected at ca. 374 nm[24] and is, thus, overlaid with features of the ruthenium(II) complexes. Both polymeric films showed weak photoluminescence. In comparison to the emission of the complexes in solution, the solid-state emission of the spin-coated monomers is bathochromically shifted by approximately 800 to 900 cm^{-1}, and the emission of the electropolymerized films is shifted by ca. 1300 cm^{-1} (see Figure 7). The spectral shifts towards higher wavelengths were observed likewise for ruthenium(II) polypyridyl systems in previous studies and are assigned to the presence of low-energy trap sites, which are available through electronic interaction between the ligand π systems of the closely packed complexes in the solid state.[26] For the polymerized systems, an even more efficient interaction is plausible and leads to the more pronounced redshift. However, no significant effect of the conjugation path on the excited-state properties was found.

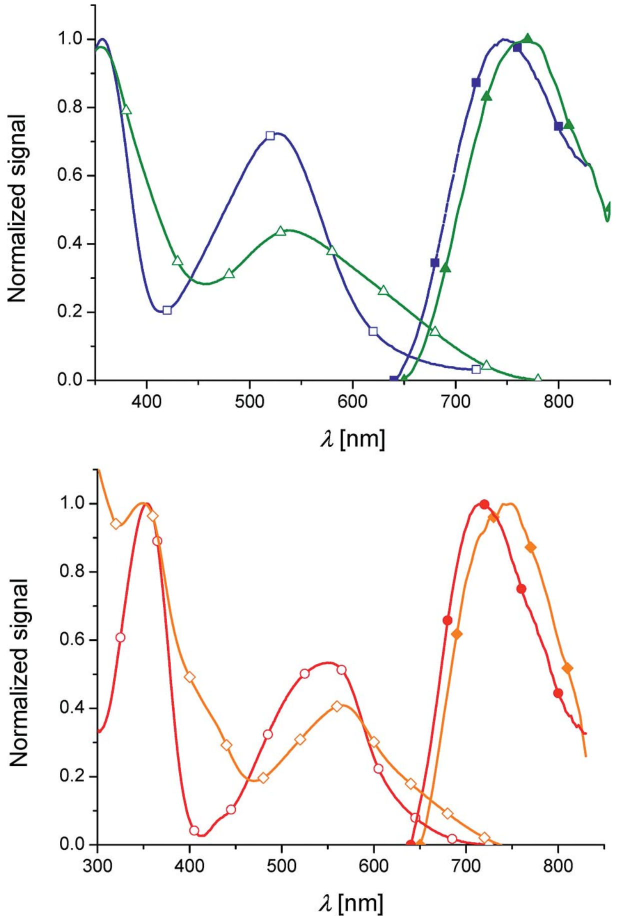

Figure 7. UV/Vis absorption (hollow symbols) and emission (filled symbols) spectra of films of poly(**1**) (green), **1** (blue) (top), poly(**2**) (orange), and **2** (red) (bottom) on ITO-coated glass substrates.

The electrosynthesized polymer films were studied by UV/Vis/NIR spectroelectrochemistry [Figure 8 shows an exemplary spectra for poly(**1**), and those of the other compounds are in the Supporting Information]. Poly(**1**) showed a bleaching of the low-energy MLCT absorption band, caused by the depletion of the respective metal-located orbitals, as well as the appearance of a broad band at 600–1100 nm, similar to that of the related monomer species. This leads to a color change of the polymer film from deep red to light yellow. However, no clear evidence of the oxidized bis(thiophene) moieties can be deduced from the data owing to the spectral overlap [the bis(phenylthienyl) radical cation absorbs at ca. 932 nm],[24] despite the occurrence of some distinct bands in comparison to $Ru(dqp)_2^{2+}$ and the respective monomers. Subsequent application of a potential

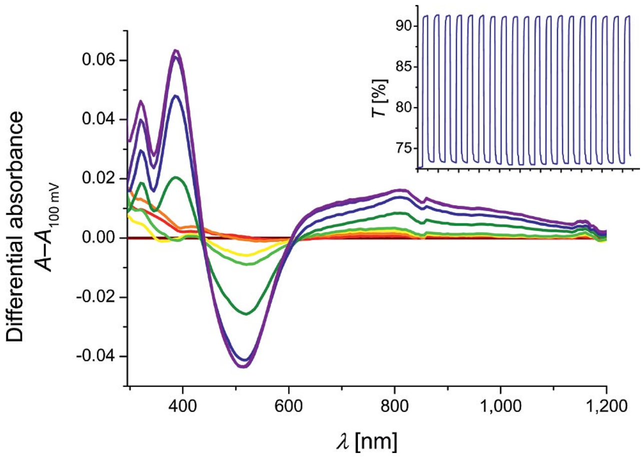

Figure 8. Exemplary change of the UV/Vis absorption spectrum of a film of poly(**1**) during the oxidation process. Inset: Change of transmission at 515 nm over 20 cycles of switching between initial and oxidized state.

able to reduce the oxidized species recovered fully the starting spectrum; the repeatable change of film transmission at 515 and 810 nm with switching potential over 20 cycles indicates a reversible and stable redox process with switching times (defined by achieving 95% of the full transmission change[27]) of approximately 2 s.

Likewise, the application of an oxidative potential to poly(**2**) films caused the disappearance of the bands between 400 and 600 nm and the increase of absorption intensity in the NIR region with a peak at 800 nm. The re-reduction of poly(**2**) produced the initial spectrum nearly completely and, at least over 20 cycles, a reversible and stable redox switching with response times of ca. 2.5 s could be observed.

Conclusions

Two new ruthenium(II) complexes based on 2,6-di(quinolin-8-yl)pyridines were synthesized by a straightforward and efficient modular route to introduce electropolymerizable 2-thienyl units. The linear arrangement within the heteroleptic and homoleptic complexes assures identical spatial separation of the metal centers within the rodlike type II (lateral incorporation) and type III (incorporation into the backbone) metallopolymers.

The monomer complexes were structurally investigated by X-ray crystallography and show a sizeable deviation from the ideal linear arrangement. The principle physicochemical characteristics of the incorporated $Ru(dqp)_2^{2+}$ moiety were preserved, that is, broad and strong long-wavelength UV/Vis absorption features, photoluminescence quantum yields up to 3% as well as reversible redox processes. Both monomers allowed well-defined potentiodynamic electropolymerization in the presence of a Lewis acid to directly yield insoluble polymer films on the electrode surfaces. The (spectro)electrochemical measurements confirmed the stability of the films towards oxidation and revealed reversible redox-triggered switching of their optical properties. A small difference between both conjugation paths was observed, namely a faster electrochemical response, which is attributed to a higher charge-carrier mobility for the type III polymer (obtained from the homoleptic monomer complex); this finding is in accordance with the higher film growth rate and DFT calculations, which revealed a more efficient π conjugation within the type III system.

However, additional parameters (e.g., counterion mobility, film morphology, and thickness) may also contribute and are under investigation. The presented approach to photoredox-active films benefits from facile instrumentation, the modular design of the monomers, and the preservation of photophysical and electrochemical properties.

Experimental Section

General Methods: All starting materials were purchased from commercial sources [dba is dibenzylideneacetone, S-PHOS is dicyclohexyl(2′,6′-dimethoxybiphenyl-2-yl)phosphane, Pd/C is activated palladium on charcoal (10 wt.-% from Aldrich)] and were used as obtained unless otherwise noted; potassium 2-nitrobenzoate,[19] 8,8′-[4-(4-bromophenyl)pyridine-2,6-diyl]diquinoline,[21] and $[Ru(dqp)(MeCN)_3](PF_6)_2$[11a,21] were prepared according to literature procedures. Flash column chromatography was conducted with a Biotage Isolera One System with Biotage SNAP Cartridges KP-Sil and a UV/Vis detector. Microwave reactions were performed with a Biotage Initiator Sixty Microwave synthesizer.

UV/Vis absorption spectra of solutions and films were recorded with a Perkin–Elmer Lambda 750 UV/Vis spectrophotometer, emission spectra of solutions were recorded with a Jasco FP6500, and emission spectra of films were recorded with a Tecan infinite M200 Pro microplate reader. Solution measurements were performed by using concentrations of 10^{-6} M in respective solvents (spectroscopy grade; deaerated for emission measurements) in 1 cm quartz cuvettes at 25 °C; emission spectra were taken by excitation at the longest-wavelength absorption maximum.

Electrochemical measurements were performed with a Metrohm Autolab PGSTAT30 potentiostat with a standard three-electrode configuration (a glassy carbon disk working electrode, a platinum-rod auxiliary electrode, and a Ag/AgCl reference electrode); scan rates from 20 to 2000 $mV\,s^{-1}$ were applied. The experiments were performed at concentrations of 10^{-4} M in degassed solvents (spectroscopy grade) containing 0.1 M Bu_4NPF_6 (dried previously by heating at 110 °C and stored under vacuum). At the end of each measurement, ferrocene was added as an internal standard.

Electropolymerization experiments were executed with the same set-up by using either a glassy carbon disk electrode or an ITO-coated glass slide (Sigma Aldrich, 0.5 × 1") as working electrode. The polymerization was performed potentiodynamically by applying velocities of 200 $mV\,s^{-1}$.

Spectroelectrochemical experiments were performed in a thin-layer quartz cuvette containing a 0.1 M Bu_4NPF_6 dichloromethane solution with an ITO-coated glass slide with the deposited polymer as the working electrode, a platinum wire auxiliary electrode, and a Ag/AgCl reference electrode. The potential was controlled by using a Metrohm Autolab PGSTAT30 potentiostat. The oxidation process was monitored by UV/Vis spectroscopy by using a Perkin–Elmer Lambda 750 UV/Vis spectrophotometer and was considered complete when there were no further spectral changes.

For comparison, films of the monomer complexes were prepared by spin-coating solutions of the monomers (5 mg mL^{-1} in acetonitrile) with a spin coater from Laurell Technologies Corporation (30 s at 1500 rpm) onto ITO-coated glass substrates (Sigma Aldrich, 1 × 1").

NMR spectra were recorded with a 250 or 300 MHz NMR spectrometer (Bruker AVANCE) with samples in deuterated solvents at 25 °C, if not noted otherwise. Chemical shifts are reported in parts per million (ppm, δ scale) relative to the residual solvent signal.[28]

ESI HRMS spectrometry was performed with an ESI-(Q)-TOF-MS MICROTOF II (Bruker Daltonics GmbH) mass spectrometer.

X-ray photoelectron spectra were recorded with an EA200-ESCA system (SPECS) by using a non-monochromatic Al-K_α radiation source ($h\upsilon$ = 1486.6 eV).

2,6-Bis(2-nitrophenyl)pyridine (3): A flask was charged with potassium 2-nitrobenzoate (13.171 g, 64.2 mmol), 2,6-dibromopyridine (6.901 g, 29.1 mmol), Pd/C (0.340 g, 0.287 mmol), copper(I) iodide (0.380 g, 1.995 mmol), 1,10-phenanthroline (0.367 g, 2.037 mmol), and *N*-methyl-2-pyrrolidinone (20 mL). The reaction mixture was heated to 180 °C for 15 h and allowed to cool to room temperature. The reaction mixture was quenched by addition of water and extracted three times with dichloromethane. The combined organic layers were dried with sodium sulfate, filtered, and the excess solvent was removed under reduced pressure (20 mbar) at 70 °C. The crude product was adsorbed on silica and purified by flash chromatography (silica gel, SNAP 50 g, eluted with hexane/CH_2Cl_2, 30:70 to 0:100, followed by evaporation of solvent under reduced pressure) to yield **3** (4.501 g, 14.01 mmol, 48%). ^{1}H NMR (CD_2Cl_2, 300 MHz): δ = 7.89 (t, J = 7.8 Hz, 1 H), 7.86 (d, J = 7.8 Hz, 2 H), 7.71–7.61 (m, 4 H), 7.55 (td, J = 7.5, 2.0 Hz, 2 H), 7.49 (d, J = 7.9 Hz, 2 H) ppm. ^{13}C NMR (CD_2Cl_2, 75 MHz): δ = 155.3, 149.3, 137.8, 134.7, 132.7, 131.5, 129.5, 124.4, 122.0 ppm. HRMS (ESI): calcd. for $C_{17}H_{11}N_3O_4Na$ [M + Na]$^+$ 344.0642; found 344.0658. $C_{17}H_{11}N_3O_4$ (321.29): calcd. C 63.55, H 3.45, N 13.08; found C 63.31, H 3.39, N 12.91.

2,2′-(Pyridine-2,6-diyl)dianiline (4): A flask was charged with **3** (4.501 g, 14.01 mmol), Pd/C (0.100 g, 0.084 mmol), ethanol (60 mL), and hydrazine hydrate (3 mL, 61.5 mmol) in portions. The reaction mixture was heated to 80 °C for 1 h. The reaction mixture was allowed to cool to room temperature, filtered, and the remaining solid was washed with dichloromethane. The filtrates were combined, and the excess solvent was removed under reduced pressure to yield **4** (3.150 g, 12.05 mmol, 86%). ^{1}H NMR (CD_2Cl_2, 300 MHz): δ = 7.87 (t, J = 8.0 Hz, 1 H), 7.53 (d, J = 8.0 Hz, 2 H), 7.52 (dd, J = 7.8, 1.3 Hz, 2 H), 7.17 (td, J = 7.7, 1.4 Hz, 2 H), 6.80–6.72 (m, 4 H), 5.32 (br. s, 4 H) ppm. ^{13}C NMR (CD_2Cl_2, 75 MHz): δ = 157.8, 146.3, 138.2, 130.0, 129.8, 122.8, 120.1, 117.6, 116.9 ppm. HRMS (ESI): calcd. for $C_{17}H_{16}N_3$ [M + H]$^+$ 284.1158; found 284.1092. $C_{17}H_{15}N_3$ (261.33): calcd. C 78.13, H 5.59, N 16.08; found C 77.77, H 5.68, N 16.07.

2,6-Bis[4-(4-bromophenyl)quinolin-8-yl]pyridine (5): A flask was charged with **4** (0.400 g, 1.531 mmol), arsenic pentoxide (1.055 g, 4.59 mmol), and phosphoric acid (85%, 15 mL). The reaction mixture was heated to 100 °C to form a yellow solution, and 1-(4-bromophenyl)-3-chloropropan-1-one (0.871 g, 3.52 mmol) was added in portions. After 30 min, the reaction mixture was heated to 140 °C for 2 h. The mixture was cooled to room temperature, neutralized by dropwise addition of aqueous sodium hydroxide (to pH 8), and extracted three times with dichloromethane. The combined organic layers were washed with water and brine, dried with sodium sulfate, filtered, and adsorbed on silica. The excess solvent was removed under reduced pressure. The crude product was purified by flash chromatography (silica gel, SNAP 50 g, adsorbed on silica, eluted with a gradient of hexane/EtOAc, 10:90 to 0:100, followed by evaporation of solvent under reduced pressure). The solid was triturated and heated to reflux in ethanol; the solids were collected from the hot solution by filtration. The obtained solids were dried under reduced pressure to yield **5** (0.150 g, 0.233 mmol, 15%).[29] ^{1}H NMR (CD_2Cl_2, 300 MHz): δ = 8.97 (d, J = 4.3 Hz, 2 H), 8.19 (dd, J = 7.1, 1.3 Hz, 2 H), 8.06 (d, J = 7.8 Hz, 2 H), 7.92 (dd, J = 8.5, 1.5 Hz, 2 H), 7.92 (dd, J = 8.4, 7.2 Hz, 2 H), 7.69 (dm, J = 8.4 Hz, 4 H), 7.62 (dd, J = 8.3, 7.3 Hz, 2 H), 7.44 (dm, J = 8.4 Hz, 4 H), 7.36 (d, J = 4.3 Hz, 2 H) ppm. ^{13}C NMR (CD_2Cl_2, 75 MHz): δ = 157.1, 149.8, 147.5, 146.6, 140.0, 137.5, 134.5, 131.9, 131.5, 131.3, 127.0, 126.7, 126.4, 125.7, 122.8, 121.4 ppm. HRMS (ESI): [M + H]$^+$ calcd. for $C_{35}H_{22}{}^{79}Br^{81}BrN_3$ 644.0158; found 644.0080.

[Ru(5)(dqp)](PF$_6$)$_2$ (6): A flask was charged with [Ru(dqp)-($CH_3CN)_3$](PF$_6$)$_2$ (0.165 g, 0.156 mmol), **5** (0.100 g, 0.155 mmol), and ethylene glycol (4 mL), purged with N_2 for 30 min, and heated to 140 °C for 14 h under a N_2 atmosphere. The crude reaction mixture was allowed to cool to room temperature and added dropwise into aqueous NH_4PF_6. The red solid was filtered, washed with water, and purified by column chromatography (silica, SNAP, CH_3CN/H_2O/neat KNO_3, 40:4), the red band was collected and the counterion exchanged with NH_4PF_6. Recystallization by vapor diffusion of diethyl ether into an acetonitrile solution yielded **6** (0.202 g, 0.148 mmol, 95%). ^{1}H NMR (CD_3CN, 300 MHz): δ = 8.20 (apparent td, J = 8.1, 1.2 Hz, 2 H), 8.14 (d, J = 5.5 Hz, 2 H), 8.11–8.07 (m, 4 H), 7.94 (d, J = 8.1 Hz, 2 H), 7.91 (d, J = 8.0 Hz, 4 H), 7.80 (d, J = 8.3 Hz, 4 H), 7.73 (d, J = 7.2 Hz, 2 H), 7.69–7.63 (m, 4 H), 7.50–7.39 (m, 8 H), 7.09 (dd, J = 8.2, 5.5 Hz, 2 H), 7.01 (d, J = 5.3 Hz, 2 H) ppm. ^{13}C NMR (CD_3CN, 75 MHz): δ = 159.6, 158.8, 157.9, 157.7, 149.4, 148.0, 147.8, 139.4, 139.2, 138.8, 136.2, 134.2, 133.9, 133.2, 133.1, 133.1, 132.6, 131.9, 129.3, 129.2, 129.2, 128.1, 127.8, 127.8, 125.8, 124.4, 123.3, 123.2 ppm. HRMS (ESI): calcd. for $C_{58}H_{36}{}^{79}Br^{81}BrN_6Ru$ [M – 2PF$_6$]$^{2+}$ 539.0200; found 539.0232.

[Ru{2,6-bis(4-{4-(thiophen-2-yl)phenyl}quinolin-8-yl)pyridine}(dqp)]-(PF$_6$)$_2$ (1): A microwave vial was charged with **6** (0.117 g, 0.086 mmol), thiophen-2-ylboronic acid (0.043 g, 0.336 mmol), Pd(dba)$_2$ (0.0025 mg, 4.35 µmol), dicyclohexyl(2′,6′-dimethoxybiphenyl-2-yl)phosphane (0.0035 g, 8.53 µmol), and potassium carbonate (0.076 g, 0.550 mmol). After the addition of acetonitrile (3 mL) and water (1.5 mL), the vial was sealed, purged for 10 min with N_2, and conventionally heated to 100 °C for 16 h. The crude reaction mixture was allowed to cool to room temperature and was purified as described for **6** to yield **1** (0.108 g, 0.079 mmol, 92%). ^{1}H NMR (CD_3CN, 250 MHz): δ = 8.22 (t, J = 8.1 Hz, 1 H), 8.21 (t, J = 8.1 Hz, 1 H), 8.14–8.05 (m, 6 H), 7.99–7.85 (m, 10 H), 7.74 (d, J = 8.1 Hz, 4 H), 7.69 (d, J = 8.2 Hz, 2 H), 7.58 (d, J = 3.6 Hz, 2 H), 7.56–7.39 (m, 10 H), 7.19 (dd, J = 4.9, 3.6 Hz, 2 H), 7.10 (dd, J = 8.1, 5.1 Hz, 2 H), 7.04 (d, J = 5.5 Hz, 2 H) ppm. ^{13}C NMR (CD_3CN, 62 MHz): δ = 159.5, 158.8, 157.9, 157.8, 150.0, 148.0, 147.8, 143.8, 139.4, 139.2, 138.8, 136.3, 136.1, 134.2, 133.9, 133.3, 133.2, 131.9, 131.6, 129.8, 129.4, 129.3, 129.2, 127.9, 127.8, 127.8, 127.4, 127.0, 125.9, 125.5, 123.2, 123.2 ppm. HRMS (ESI): calcd. for $C_{66}H_{42}N_6RuS$ [M – 2PF$_6$]$^{2+}$ 542.0981; found 542.1057.

[Ru(8,8′-{4-(4-bromophenyl)pyridine-2,6-diyl}diquinoline)$_2$-($CH_3CN)_3$](PF$_6$)$_2$ (7): A microwave vial was charged with 8,8′-[4-(4-bromophenyl)pyridine-2,6-diyl]diquinoline[21] (0.300 g, 0.614 mmol), ruthenium trichloride hydrate (0.164 g, 0.585 mmol), and ethanol (10 mL). The vial was sealed and conventionally heated to 115 °C for 13 h. The reaction mixture was allowed to cool to room temperature, filtered, and washed thoroughly with ethanol and dichloromethane. The dark brown solid was dried under reduced pressure to yield crude Ru{8,8′-[4-(4-bromophenyl)-pyridine-2,6-diyl]diquinoline}Cl_3 (0.352 g, 0.506 mmol, 86 %).

A flask was charged with crude Ru{8,8′-[4-(4-bromophenyl)pyridine-2,6-diyl]diquinoline}Cl_3 (0.352 g, 0.506 mmol), silver nitrate (0.301 g, 1.771 mmol), acetonitrile (7 mL), ethanol (1.5 mL), and water (1.5 mL). The suspension was heated to 90 °C for 17 h. The white solids were removed by filtration, and the orange-brown solution was reduced in volume under reduced pressure and purified as described for **6** to yield **7** (0.305 g, 0.304 mmol, 60 %). ^{1}H NMR (CD_3CN, 300 MHz): δ = 9.08 (dd, J = 5.2, 1.2 Hz, 2 H), 8.67 (br. d, J = 7.5 Hz, 2 H), 8.62 (dd, J = 8.4, 1.2 Hz, 2 H), 8.28 (d, J = 8.2 Hz, 2 H), 8.18 (s, 2 H), 7.93 (t, J = 7.8 Hz, 2 H), 7.87 (dm, J = 8.5 Hz, 2 H), 7.77 (dm, J = 8.5 Hz, 2 H), 7.67 (dd, J = 8.2, 5.2 Hz, 2 H), 2.45 (s, 3 H), 1.96 (s, 6 H) ppm. ^{13}C NMR (CD_3CN, 63 MHz): δ = 159.8, 158.6, 150.0, 147.3, 139.7, 136.2, 135.3, 135.2, 133.5, 133.0, 130.4, 129.7, 129.2, 127.8, 127.3, 126.3, 125.5, 123.2, 4.5, 3.8 ppm. HRMS (ESI): calcd. for $C_{35}H_{27}{}^{79}BrN_6Ru$ [M – $2PF_6]^{2+}$ 356.0259; found 355.8804.

[Ru{8,8′-(4-{4-(thiophen-2-yl)phenyl}pyridine-2,6-diyl)diquinoline}$_2$]-(PF_6)$_2$ (2): A flask was charged with **7** (0.195 g, 0.195 mmol), 8,8′-[4-(4-bromophenyl)pyridine-2,6-diyl]diquinoline (0.095 g, 0.195 mmol), and ethylene glycol (10 mL) and heated to 140 °C under N_2 for 14 h. The crude reaction mixture was allowed to cool to room temperature and was worked up as described for **6** to yield crude [Ru(8,8′-{4-(4-bromophenyl)pyridine-2,6-diyl}diquinoline)$_2$](PF_6)$_2$ containing some monodebrominated product (0.180 g, 0.132 mmol, 68 %).

A microwave vial was charged with crude [Ru(8,8′-{4-(4-bromophenyl)pyridine-2,6-diyl}diquinoline)$_2$](PF_6)$_2$ (0.180 g, 0.132 mmol), thiophen-2-ylboronic acid (0.067 g, 0.526 mmol), Pd(dba)$_2$ (0.0038 g, 6.58 µmol), dicyclohexyl(2′,6′-dimethoxybiphenyl-2-yl)phosphane (0.0054 g, 0.013 mmol), and potassium carbonate (0.111 g, 0.790 mmol). After the addition of acetonitrile (3 mL) and water (1.5 mL), the vial was sealed, purged for 10 min with N_2, and conventionally heated to 100 °C for 16 h. The reaction mixture was worked up as described for **6** to yield the title compound **2** (0.100 g, 0.073 mmol, 55 %). ^{1}H NMR (CD_3CN, 300 MHz): δ = 8.18–8.13 (m, 8 H), 8.09 (dd, J = 8.1, 1.2 Hz, 4 H), 8.01 (d, J = 8.5 Hz, 4 H), 7.93 (dd, J = 7.4, 1.2 Hz, 4 H), 7.88 (d, J = 8.5 Hz), 7.72 (dd, J = 8.2, 1.2 Hz, 4 H), 7.58 (dd, J = 3.6, 1.0 Hz, 2 H), 7.50 (t, J = 7.5 Hz, 4 H), 7.50 (dd, J = 5.1, 1.0 Hz, 2 H), 7.18 (dd, J = 5.1, 3.7 Hz, 2 H), 7.09 (dd, J = 8.2, 5.2 Hz, 4HH) ppm. ^{13}C NMR (CD_3CN, 75 MHz): δ = 159.6, 158.1, 149.8, 147.7, 143.7, 138.6, 137.2, 135.8, 134.5, 133.0, 131.6, 129.7, 129.2, 127.9, 127.6, 127.5, 127.4, 126.1, 125.7, 123.1 ppm. HRMS (ESI): calcd. for $C_{66}H_{42}N_6RuS_2$ [M – $2PF_6]^{2+}$ 542.0981; found 542.0990.

X-ray Crystallography: The intensity data for the compounds were collected with a Nonius KappaCCD diffractometer with graphite-monochromated Mo-K_α radiation. The data were corrected for Lorentz and polarization effects but not for absorption effects.[30]

The structures were solved by direct methods (SHELXS[31]) and refined by full-matrix least-squares techniques against $F_o{}^2$ (SHELXL-97[31]). All hydrogen atoms were included at calculated positions with fixed thermal parameters. All non-hydrogen, non-disordered atoms were refined anisotropically.[31] The crystals of **1** were extremely thin and of low quality and resulted in a substandard data set; however, the structure is sufficient to show the connectivity and geometry despite the high final R value. We will only publish the conformation of the molecule and the crystallographic data. We will not deposit the data in the Cambridge Crystallographic Data Centre. Crystallographic data as well as structure solution and refinement details are summarized in the Supporting Information. XP (Siemens Analytical X-ray Instruments, Inc.) was used for structure representations.

CCDC-888462 (for **6**) and -888463 (for **2**) contain the supplementary crystallographic data for this paper. These data can be obtained free of charge from The Cambridge Crystallographic Data Centre via www.ccdc.cam.ac.uk/data_request/cif.

Computational Methods: All calculations were performed with the Gaussian 09 (G09) program package[32] by employing the DFT method and using Becke's three-parameter hybrid functional[33] and the Lee–Yang–Parr gradient-corrected correlation functional[34] (B3LYP). The ruthenium atoms were treated by the 28-electron relativistic effective core potential MWB[35] for the inner shells, whereas the outer shells (4s, 4p, 4d, and 5s electrons) were treated separately. The remaining atoms (C, H, N, and S) were treated with the 6-31G(d) double-ζ basis set.[36] Bulk solvent effects (acetonitrile) were included by using the integral equation formalism of the polarizable continuum model of Tomasi and coworkers.[37] The geometry optimizations of the singlet and triplet states were performed without any constraints and the true nature was confirmed by normal-mode analysis. The molecular orbitals and electron/spin densities were visualized by using the GaussView 5.0 package.[38] The vertical excitations were computed by TD-DFT at the same level of theory. The electronic transitions were determined from the changes in electronic distribution by using electron-density difference maps (EDDMs),[39] which were computed with the GaussSum 2.2 package.[40] The triplet excited states were visualized by spin-density plots, expressed as a difference between α and β spin densities, by using the GaussView 5.0 package.[38] The density of states (DOS) and crystal orbital overlap population (COOP) analysis was performed by using the GaussSum 2.2 package.[40]

Supporting Information (see footnote on the first page of this article): Spectral data (UV/Vis, UV/Vis/NIR spectroelectrochemistry, XPS), DFT calculation results, and X-ray crystallographic data.

Acknowledgments

The authors acknowledge the Bundesministerium für Bildung und Forschung, the European Social Fund (ESF), the Thüringer Aufbaubank (TAB), and the Thuringian Ministry of Economy, Employment and Technology (TMWAT) for financial support. M. J. is grateful for financial support from the Carl-Zeiss-Stiftung. The authors also thank Esra Altuntas for ESI measurements and Dr. Bernd Schröter for XPS measurements.

---

[1] a) A. Juris, V. Balzani, F. Barigelletti, S. Campagna, P. Belser, A. von Zelewsky, *Coord. Chem. Rev.* **1988**, *84*, 85–277; b) T. J. Meyer, *Pure Appl. Chem.* **1986**, *58*, 1193–1206.

[2] B. Durham, J. V. Caspar, J. K. Nagle, T. J. Meyer, *J. Am. Chem. Soc.* **1982**, *104*, 4803–4810.

[3] J.-P. Sauvage, J.-P. Collin, J.-C. Chambron, S. Guillerez, C. Coudret, V. Balzani, F. Barigelletti, L. De Cola, L. Flamigni, *Chem. Rev.* **1994**, *94*, 993–1019.

[4] a) E. C. Constable, *Chem. Soc. Rev.* **2007**, *36*, 246–253; b) H. Hofmeier, U. S. Schubert, *Chem. Soc. Rev.* **2004**, *33*, 373–399.

[5] J. R. Winkler, T. L. Netzel, C. Creutz, N. Sutin, *J. Am. Chem. Soc.* **1987**, *109*, 2381–2392.

[6] a) B. Schulze, D. Escudero, C. Friebe, R. Siebert, H. Görls, S. Sinn, M. Thomas, S. Mai, J. Popp, B. Dietzek, L. González, U. S. Schubert, *Chem. Eur. J.* **2012**, *18*, 4010–4025; b) O. A.

Borg, S. S. M. C. Godinho, M. J. Lundqvist, S. Lunell, P. Persson, *J. Phys. Chem. A* **2008**, *112*, 4470–4476; c) A. Amini, A. Harriman, A. Mayeux, *Phys. Chem. Chem. Phys.* **2004**, *6*, 1157–1164; d) D. W. Fink, W. E. Ohnesorge, *J. Am. Chem. Soc.* **1969**, *91*, 4995–4998.

[7] a) M. Jäger, A. Smeigh, F. Lombeck, H. Görls, J.-P. Collin, J.-P. Sauvage, L. Hammarström, O. Johansson, *Inorg. Chem.* **2010**, *49*, 374–376; b) S. H. Wadman, M. Lutz, D. M. Tooke, A. L. Spek, F. Hartl, R. W. A. Havenith, G. P. M. van Klink, G. van Koten, *Inorg. Chem.* **2009**, *48*, 1887–1900; c) P. G. Bomben, K. C. D. Robson, P. A. Sedach, C. P. Berlinguette, *Inorg. Chem.* **2009**, *48*, 9631–9643; d) J.-P. Collin, M. Beley, J.-P. Sauvage, F. Barigelletti, *Inorg. Chim. Acta* **1991**, *186*, 91–93.

[8] a) H.-J. Park, K. H. Kim, S. Y. Choi, H.-M. Kim, W. I. Lee, Y. K. Kang, Y. K. Chung, *Inorg. Chem.* **2010**, *49*, 7340–7352; b) B. Schulze, D. Escudero, C. Friebe, R. Siebert, H. Görls, U. Köhn, E. Altuntas, A. Baumgaertel, M. D. Hager, A. Winter, B. Dietzek, J. Popp, L. González, U. S. Schubert, *Chem. Eur. J.* **2011**, *17*, 5494–5498.

[9] a) L. Hammarström, O. Johansson, *Coord. Chem. Rev.* **2010**, *254*, 2546–2559; b) A. Breivogel, C. Förster, K. Heinze, *Inorg. Chem.* **2010**, *49*, 7052–7056; c) F. Schramm, V. Meded, H. Fliegl, K. Fink, O. Fuhr, Z. Qu, W. Klopper, S. Finn, T. E. Keyes, M. Ruben, *Inorg. Chem.* **2009**, *48*, 5677–5684.

[10] a) J. Wang, Y.-Q. Fang, L. Bourget-Merle, M. I. J. Polson, G. S. Hanan, A. Juris, F. Loiseau, S. Campagna, *Chem. Eur. J.* **2006**, *12*, 8539–8548; b) J. Wang, G. S. Hanan, F. Loiseau, S. Campagna, *Chem. Commun.* **2004**, 2068–2069.

[11] a) M. Jäger, R. J. Kumar, H. Görls, J. Bergquist, O. Johansson, *Inorg. Chem.* **2009**, *48*, 3228–3238; b) M. Abrahamsson, M. Jäger, T. Österman, L. Eriksson, P. Persson, H.-C. Becker, O. Johansson, L. Hammarström, *J. Am. Chem. Soc.* **2006**, *128*, 12616–12617.

[12] a) C. Friebe, M. D. Hager, A. Winter, U. S. Schubert, *Adv. Mater.* **2012**, *24*, 332–345; b) M. O. Wolf, *J. Inorg. Organomet. Polym. Mater.* **2006**, *16*, 189–199.

[13] a) Y.-W. Zhong, C.-J. Yao, H.-J. Nie, *Coord. Chem. Rev.* **2013**, *257*, 1357–1372; b) C.-J. Yao, Y.-W. Zhong, H.-J. Nie, H. D. Abruña, J. Yao, *J. Am. Chem. Soc.* **2011**, *133*, 20720–20723; c) X. J. Zhu, B. J. Holliday, *Macromol. Rapid Commun.* **2010**, *31*, 904–909; d) J. Hjelm, R. W. Handel, A. Hagfeldt, E. C. Constable, C. E. Housecroft, R. J. Forster, *Inorg. Chem.* **2005**, *44*, 1073–1081; e) R. M. Leasure, T. Kajita, T. J. Meyer, *Inorg. Chem.* **1996**, *35*, 5962–5963; f) C. P. Horwitz, Q. Zuo, *Inorg. Chem.* **1992**, *31*, 1607–1613; g) T. F. Guarr, F. C. Anson, *J. Phys. Chem.* **1987**, *91*, 4037–4043; h) C. D. Ellis, L. D. Margerum, R. W. Murray, T. J. Meyer, *Inorg. Chem.* **1983**, *22*, 1283–1291; i) P. Denisevich, H. D. Abruña, C. R. Leidner, T. J. Meyer, R. W. Murray, *Inorg. Chem.* **1982**, *21*, 2153–2161.

[14] M. O. Wolf, *Adv. Mater.* **2001**, *13*, 545–553.

[15] a) M. L. Naklicki, S. I. Gorelsky, W. Kaim, B. Sarkar, R. J. Crutchley, *Inorg. Chem.* **2012**, *51*, 1400–1407; b) M. Lundberg, P. E. M. Siegbahn, *J. Chem. Phys.* **2005**, *122*, 224103.

[16] Y. Sun, M. El Ojaimi, R. Hammitt, R. P. Thummel, C. Turro, *J. Phys. Chem. B* **2010**, *114*, 14664–14670.

[17] J. Heinze, B. A. Frontana-Uribe, S. Ludwigs, *Chem. Rev.* **2010**, *110*, 4724–4771.

[18] L. J. Goossen, N. Rodríguez, B. Melzer, C. Linder, G. Deng, L. M. Levy, *J. Am. Chem. Soc.* **2007**, *129*, 4824–4833.

[19] L. J. Gooßen, B. Zimmermann, C. Linder, N. Rodríguez, P. P. Lange, J. Hartung, *Adv. Synth. Catal.* **2009**, *351*, 2667–2674.

[20] D. Pomeranc, V. Heitz, J.-C. Chambron, J.-P. Sauvage, *J. Am. Chem. Soc.* **2001**, *123*, 12215–12221.

[21] M. Jäger, L. Eriksson, J. Bergquist, O. Johansson, *J. Org. Chem.* **2007**, *72*, 10227–10230.

[22] S. Jin, G. Xue, *Macromolecules* **1997**, *30*, 5753–5757.

[23] P. J. Hochgesang, R. D. Bereman, *Inorg. Chim. Acta* **1988**, *149*, 69–76.

[24] J. J. Apperloo, L. B. Groenendaal, H. Verheyen, M. Jayakannan, R. A. J. Janssen, A. Dkhissi, D. Beljonne, R. Lazzaroni, J.-L. Brédas, *Chem. Eur. J.* **2002**, *8*, 2384–2396.

[25] a) A. J. Bard, L. R. Faulkner, *Electrochemical Methods*, 2nd ed., John Wiley & Sons, New York, **2001**; b) the relationship between the peak current and scan rate may also be strongly influenced by film thickness.

[26] a) M. Devenney, L. A. Worl, S. Gould, A. Guadalupe, B. P. Sullivan, J. V. Caspar, R. L. Leasure, J. R. Gardner, T. J. Meyer, *J. Phys. Chem. A* **1997**, *101*, 4535–4540; b) J. L. Colón, C. Y. Yang, A. Clearfield, C. R. Martin, *J. Phys. Chem.* **1988**, *92*, 5777–5781.

[27] C. L. Gaupp, D. M. Welsh, R. D. Rauh, J. R. Reynolds, *Chem. Mater.* **2002**, *14*, 3964–3970.

[28] H. E. Gottlieb, V. Kotlyar, A. Nudelman, *J. Org. Chem.* **1997**, *62*, 7512–7515.

[29] A small amount of inseparable impurities remained and were readily removed after the coordination step.

[30] a) *COLLECT, Data Collection Software*, Nonius B. V., The Netherlands, **1998**; b) Z. Otwinowski, W. Minor, in: *Processing of X-ray diffraction data collected in oscillation mode*, in: *Methods in Enzymology*, vol. 276: *Macromolecular Crystallography*, Part A (Eds.: C. W. Carter, R. M. Sweet), Academic Press, New York, **1997**, p. 307–326.

[31] G. M. Sheldrick, *Acta Crystallogr., Sect. A* **2008**, *64*, 112–122.

[32] M. J. Frisch, G. W. Trucks, H. B. Schlegel, G. E. Scuseria, M. A. Robb, J. R. Cheeseman, G. Scalmani, V. Barone, B. Mennucci, G. A. Petersson, H. Nakatsuji, M. Caricato, X. Li, H. P. Hratchian, A. F. Izmaylov, J. Bloino, G. Zheng, J. L. Sonnenberg, M. Hada, M. Ehara, K. Toyota, R. Fukuda, J. Hasegawa, M. Ishida, T. Nakajima, Y. Honda, O. Kitao, H. Nakai, T. Vreven, J. A. Montgomery Jr., J. E. Peralta, F. Ogliaro, M. Bearpark, J. J. Heyd, E. Brothers, K. N. Kudin, V. N. Staroverov, R. Kobayashi, J. Normand, K. Raghavachari, A. Rendell, J. C. Burant, S. S. Iyengar, J. Tomasi, M. Cossi, N. Rega, J. M. Millam, M. Klene, J. E. Knox, J. B. Cross, V. Bakken, C. Adamo, J. Jaramillo, R. Gomperts, R. E. Stratmann, O. Yazyev, A. J. Austin, R. Cammi, C. Pomelli, J. W. Ochterski, R. L. Martin, K. Morokuma, V. G. Zakrzewski, G. A. Voth, P. Salvador, J. J. Dannenberg, S. Dapprich, A. D. Daniels, Ö. Farkas, J. B. Foresman, J. V. Ortiz, J. Cioslowski, D. J. Fox, *Gaussian 09*, revision A.1, Gaussian, Inc., Wallingford, **2009**.

[33] A. D. Becke, *J. Chem. Phys.* **1993**, *98*, 5648–5652.

[34] C. T. Lee, W. T. Yang, R. G. Parr, *Phys. Rev. B* **1988**, *37*, 785–789.

[35] D. Andrae, U. Häußermann, M. Dolg, H. Stoll, H. Preuß, *Theor. Chim. Acta* **1990**, *77*, 123–141.

[36] P. C. Hariharan, J. A. Pople, *Theor. Chim. Acta* **1973**, *28*, 213–222.

[37] J. Tomasi, B. Mennucci, R. Cammi, *Chem. Rev.* **2005**, *105*, 2999–3094.

[38] *GaussView*, v. 5.0.8, R. D. Dennington, T. A. Keith, J. M. Millan, Semicchem, Inc., Shawnee KS, **2008**.

[39] W. R. Browne, N. M. O'Boyle, J. J. McGarvey, J. G. Vos, *Chem. Soc. Rev.* **2005**, *34*, 641–663.

[40] a) *GaussSum*, v. 2.2.5, N. M. O'Boyle, J. G. Vos, Dublin City University, Dublin, Ireland, **2009**; available at http://gausssum.sourceforge.net ; b) N. M. O'Boyle, A. L. Tenderholt, K. M. Langner, *J. Comput. Chem.* **2008**, *29*, 839–845.

Received: March 15, 2013